THEORETICAL AND NUMERICAL ANALYSIS OF THE FIXED FLAT-PLATE SOLAR COLLECTOR WITH SN-AL_2O_3 SELECTIVE ABSORBER AND GRAVITY WATER FLOW

*Aleksandar M. NEŠOVIĆ[1], Nebojša S. LUKIĆ[1], Dragan Z. CVETKOVIĆ[*2],*
Miljan R. MARAŠEVIĆ[3], Marko D. TOPALOVIĆ[2]

[1] Faculty of Engineering, University of Kragujevac, Serbia

[2] Institute of Information Technologies, University of Kragujevac, Serbia

[3] Faculty of Mechanical and Civil Engineering in Kraljevo, University of Kragujevac, Serbia

[*] Corresponding author; E-mail: dragan_cw8202@yahoo.com

Abstract: This paper presents two methods (theoretical and numerical) for the thermal analysis of the previously experimentally installed solar collector construction at the Faculty of Engineering in Kragujevac – a fixed flat-plate solar collector with Sn-Al₂O₃ selective absorber and gravity water flow. The theoretical research was based on the application of a specific calculation algorithm with a triple iterative procedure, i.e. with a three-stage check of all important performance indicators of the fixed flat-plate solar collector. In the numerical phase of the research, Simple Linear Regression was applied to experimentally measured values of solar radiation intensity and experimentally determine values of heat power to form simple equations that could be used to predict the thermal performance of similar solar structures in the future. The results of theoretical and numerical studies showed agreement with experimental studies, because in the first case, the absolute measurement error was less than 10%, while in the second case, the determination coefficient was greater than 90%, so the authors hope that this work will be useful to the wider scientific community.

Keywords*: Fixed flat-plate solar collector; Gravity water flow; Numerical model; Results validation; Sn-Al₂O₃ selective absorber; Theoretical model.*

1. Introduction

Of all solar collector (*SC*) types, flat-plate solar collectors (*FPSC*) still have the greatest practical application. The construction is simple, the production cost is low, the thermal performance is satisfactory, and the field of application is wide (residential [1], and industrial [2]).

Continuous work is being done to improve this solar construction, in terms of energy, ecology, and economy. A result is a large number of modified *FPSC* models, usually theoretically and numerically investigated, and then experimentally.

To collect more incoming solar radiation (improvement of the solar incident angle [3]), modifying the *FPSC* is reflected in the application of various selective coatings of absorber plates, glass covers (single, double, and multi-layer), additional elements (concentrators, mirrors, and reflectors), and tracking system (single-axis tracking (*SAT*), and double-axis tracking (*DAT*)).

Various types of selective coatings (selective absorbers) are investigated in the following works: $Ni\text{-}Al_2O_3$ [4-6], $AlNi\text{-}Al_2O_3$ [7], $Mo\text{-}Al_2O_3$ [8, 9], $W\text{-}Al_2O_3$ [10], $Cu\text{-}CuAl_2O_4$ [11], $Pt\text{-}Al_2O_3$ [12], $Ag\text{-}Al_2O_3$ [13], and $Sn\text{-}Al_2O_3$ [14-16].

Experimental and numerical investigation of the *FPSC* with a single glass layer is presented in [17]. In [18], the optical performance (which depends on the transparency coefficient of glass and the absorption coefficient of the selective absorber) of the *FPSC* was investigated by *Hellstrom et al*. The *FPSC* with a different type of vacuum glazing [19] and with coated and uncoated glass cover [20] are investigated. On the other side, glass-cover temperatures and heat losses [21], optimization [22], and thermal performance [23] of the *FPSC* with double glazing [24] also can be found in the literature.

The theoretical model of a one-sided *FPSC* extension, using a fixed flat reflector on its lower side, for the area of Italy, is presented in [25, 26]. Using two average daily performance indices (area ratio and enhancement factor), in [27] the combination of *FPSC* with single-sided upper, single-sided lower reflector, and double-sided (upper and lower, i.e. right and left) reflectors were investigated. In all analyzed scenarios, the reflectors were fixed and flat. The *FPSC* with four-sided fixed reflectors [28] was theoretically analyzed for latitudes in the range of 35-45°, due to its eventual application during the winter season (first scenario) or throughout the year (second scenario). The paper presents methods for determining the optimal position of such a solar construction. In [29], the optimal position of a flat reflector (with manual apparent Sun tracking) under the doubly exposed *FPSC* was mathematically investigated.

A mathematical model developed in Brazil [30] showed that *FPSC* with *DAT* mechanism is a better solution than *FPSC* with *SAT*. In [31], *Neville* numerically compared the thermal performance of different concepts of the *FPSC*: *FPSC* with *SAT* in the E-W direction (first case), *FPSC* with *SAT* in the N-S direction (second case), and *FPSC* with *DAT* (third case). Similar numerical analyzes of the thermal behavior of the *FPSC* with *DAT* were carried out in [32] and [33].

As a contribution to the research of *SCs* in the field of solar technology, in this paper, the theoretical and numerical research of *fFPSC* with $Sn\text{-}Al_2O_3$ selective absorber and gravity water flow – solar construction without a circulation pump was carried out, previous experimental [34] research at the Faculty of Engineering in Kragujevac (Central Serbia).

By eliminating the additional energy investment to start the circulation pump, additional benefits are achieved without additional damage to thermal performance, with the possibility of additional expansion of the *fFPSC* application field – primarily to the agricultural sector in the moderate continental climate, and then in the industrial and residential sectors.

2. Solar design

The complete solar installation is shown in Fig. 1a. The central place is occupied by *fFPSC* (Fig. 1b) with the following elements (Fig. 1c): absorber (composed of 5 $Sn\text{-}Al_2O_3$ selective plates), single-layer glass cover, air layer (between the glass cover and absorber), insulating layer (hard-pressed mineral wool), and aluminum frame. A more detailed description of all mentioned elements is available in [34].

The solar installation in its assembly does not have a circulation pump, so instead of a closed circulation circuit, the gravitational force is used to overcome all the resistances in the relationship between the upper tank – *fFPSC* – the lower tank.
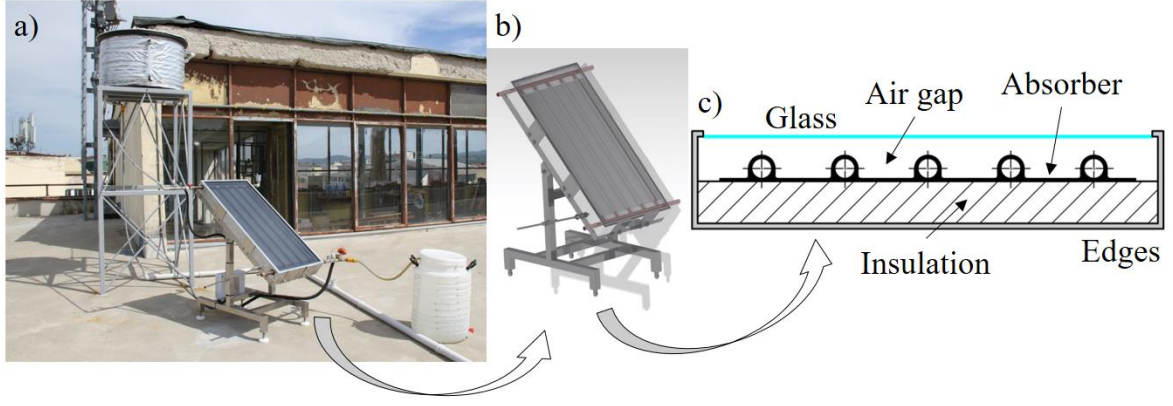
Fig. 1. Construction of the *fFPSC* with *Sn-Al₂O₃* selective absorber and gravity water flow.

3. Theoretical model

3.1. Solar incident angle

Solar incident angles for the fixed horizontal θ_z [°] Eq. (1), and the fixed tilted θ_β [°] Eq. (2) surfaces can be found in [3] (Fig. 2):

$$\cos\theta_z = \cos\varphi\cos\delta\cos\omega + \sin\varphi\sin\delta \tag{1}$$

$$\cos\theta_\beta = \cos\varphi\cos\delta\cos\omega\cos\beta + \sin\varphi\sin\delta\cos\beta + $$
$$+ \sin\varphi\cos\delta\cos\omega\sin\beta - \cos\varphi\sin\delta\sin\beta \tag{2}$$

where: φ [°] is the latitude angle, δ [°] is the declination angle, ω [°] is the hour angle, and β [°] is the inclination angle.
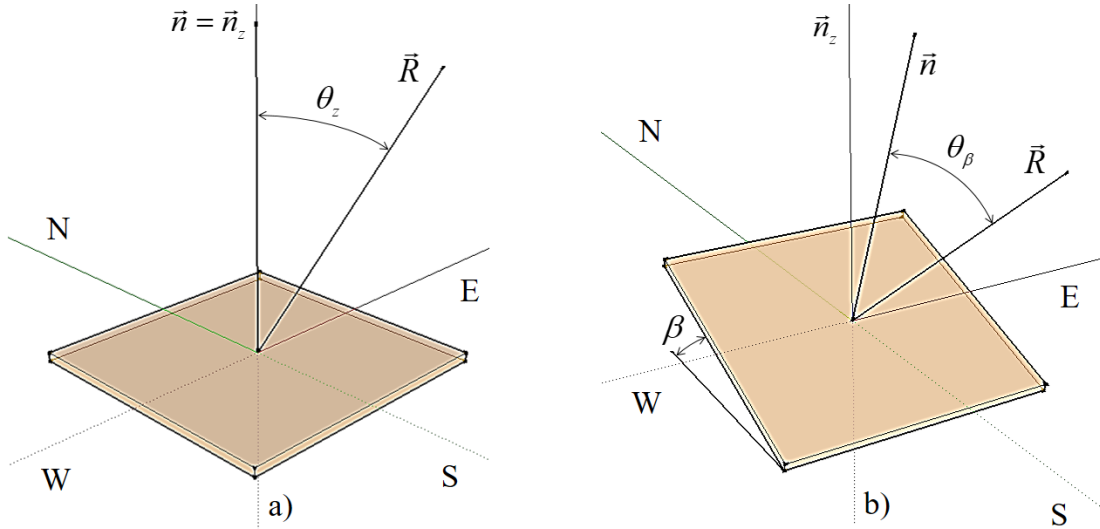
Fig. 2. Solar incident angle for the fixed horizontal (a), and fixed tilted (b) surface.
N – North; E – East; S – South; W – West; $\vec{n}_z$ – Vector normal to the ground surface;
$\vec{n}$ – Vector normal to the *fFPSC* surface; $\vec{R}$ – Sun position vector.

3.2. Optical efficiency

Authors in [35] proposed equations for the *fFPSC* optical efficiency of the beam $(\tau\alpha)_{F,BEAM}$ [-] Eq. (3), $(\tau\alpha)_{F,DIFF}$ [-] diffuse Eq. (4), and reflected $(\tau\alpha)_{F,REFL}$ [-] Eq. (5) solar radiation:

$$(\tau a)_{F,BEAM} = 1{,}01 (\tau a)_{F(\perp)} \tau_{F,B} a_{F,B} \tag{3}$$

$$(\tau a)_{F,DIFF} = 1{,}01 (\tau a)_{F(\perp)} \tau_{F,D} a_{F,D} \tag{4}$$

$$(\tau a)_{F,REFL} = 1{,}01 (\tau a)_{F(\perp)} \tau_{F,R} a_{F,R} \tag{5}$$

where: $(\tau a)_{F(\perp)}$ [-] is the nominal optical efficiency, $\tau_{F,B}$ [-] is the transmittance coefficient of the beam solar radiation depending on the solar incident angle, $\alpha_{F,B}$ [-] is the absorption coefficient of the beam solar radiation depending on the solar incident angle, $\tau_{F,D}$ [-] is the transmittance coefficient of the diffuse solar radiation depending on the solar incident angle, $\alpha_{F,D}$ [-] is the absorption coefficient of the diffuse solar radiation depending on the solar incident angle, $\tau_{F,R}$ [-] is the transmittance coefficient of the reflected solar radiation depending on the solar incident angle, and $\alpha_{F,R}$ [-] is the absorption coefficient of the reflected solar radiation depending on the solar incident angle.

3.3. Total absorbed solar radiation

According to [36], for the *fFPSC*, the total absorbed solar radiation $I_{F,TOT}$ [Wm^{-2}] Eq. (6) is the sum of the absorbed beam $I_{F,BEAM}$ [Wm^{-2}] Eq. (7), diffuse $I_{F,DIFF}$ [Wm^{-2}] Eq. (8), and reflected $I_{F,TOT}$ [Wm^{-2}] Eq. (9) solar radiation:

$$I_{F,TOT} = I_{F,BEAM} + I_{F,DIFF} + I_{F,REFL} \tag{6}$$

$$I_{F,BEAM} = (\tau a)_{F,BEAM} I_{BEAM} \frac{\cos\theta_\beta}{\cos\theta_z} \tag{7}$$

$$I_{F,DIFF} = (\tau a)_{F,DIFF} I_{DIFF} \frac{1+\cos\beta}{2} \tag{8}$$

$$I_{F,REFL} = (\tau a)_{F,REFL} \, alb_{F,REFL} \left(I_{BEAM} + I_{DIFF} \right) \frac{1-\cos\beta}{2} \tag{9}$$

where: I_{BEAM} [Wm^{-2}] is the incoming beam solar radiation, I_{DIFF} [Wm^{-2}] is the incoming diffuse solar radiation, and $alb_{F,REFL}$ [-] is the ground albedo.

3.4. Heat losses

The heat losses $Q_{F,LOSS}$ [W] Eq. (10) that occur in the *fFPSC* (Fig. 3), according to the recommendations from [37-40], can be presented using their resistance $R_{F,LOSS}$ [KW^{-1}] Eq. (11), in the following way:

$$Q_{F,LOSS} = \frac{T_{F,ABS} - T_{air}}{\sum R_{F,LOSS}} \tag{10}$$

$$\sum R_{F,LOSS} = \frac{1}{A_{F,ABS(up)} \sum U_{F,LOSS}} = \frac{1}{A_{F,ABS(up)} \left(U_{F,GL} + U_{F,INS} + U_{F,EDG} \right)} \tag{11}$$

where: $T_{F,ABS}$ [K] is the average temperature of the absorber, T_{air} [K] is the temperature of the ambient air, $A_{F,ABS(up)}$ [m^2] is the surface area of the absorber upper side, $U_{F,LOSS}$ [Wm^{-2}K^{-1}] is the heat transfer coefficient through the *fFPSC*, $U_{F,GL}$ [Wm^{-2}K^{-1}] is the heat transfer coefficient through the glass cover Eq. (12), $U_{F,INS}$ [Wm^{-2}K^{-1}] is the heat transfer coefficient through the insulation Eq. (13), and $U_{F,EDG}$ [Wm^{-2}K^{-1}] is the heat transfer coefficient for the collector edges Eq. (14).

$$U_{F,GL} = \cfrac{1}{\cfrac{1}{h_{F,ABS-GL(rad)} + h_{F,ABS-GL(con)}} + \cfrac{d_{F,GL}}{k_{F,GL}} + \cfrac{1}{h_{F,GL-air(rad)} + h_{F,GL-air(con)}}} \quad (12)$$

$$U_{F,INS} = \cfrac{1}{\cfrac{d_{F,INS}}{k_{F,INS}} + \cfrac{1}{h_{F,INS-air(con)}}} \quad (13)$$

$$U_{F,EDG} = \cfrac{1}{\cfrac{d_{F,EDG}}{k_{F,EDG}} + \cfrac{1}{h_{F,EDG-air(con)}}} \cfrac{A_{F,EDG}}{A_{F,TOT}} \quad (14)$$

where: $h_{F,ABS-GL(rad)}$ [Wm^{-2}K^{-1}] is the radiation transfer coefficient from the absorber to the glass cover, $h_{F,ABS-GL(con)}$ [Wm^{-2}K^{-1}] is the convection transfer coefficient from the absorber to the glass cover, $d_{F,GL}$ [m] is the thickness of the glass cover, $k_{F,GL}$ [Wm^{-1}K^{-1}] is the thermal conductivity of the glass cover, $h_{F,GL-air(rad)}$ [Wm^{-2}K^{-1}] is the radiation transfer coefficient from the glass cover to the ambient air, $h_{F,GL-air(con)}$ [Wm^{-2}K^{-1}] is the convection transfer coefficient from the glass cover to the ambient air, $d_{F,INS}$ [m] is the thickness of the insulation, $k_{F,INS}$ [Wm^{-1}K^{-1}] is the thermal conductivity of the insulation, $h_{F,INS-air(con)}$ [Wm^{-2}K^{-1}] is the convection transfer coefficient from the insulation to the ambient air, $d_{F,EDG}$ [m] is the thickness of the side edges, $k_{F,EDG}$ [Wm^{-1}K^{-1}] is the thermal conductivity of the side edges, $h_{F,EDG-air(con)}$ [Wm^{-2}K^{-1}] is the convection transfer coefficient from the side edges to the ambient air, $A_{F,EDG}$ [m^2] is the side edges surface area, and $A_{F,TOT}$ [m^2] is the *fFPSC* total surface area.
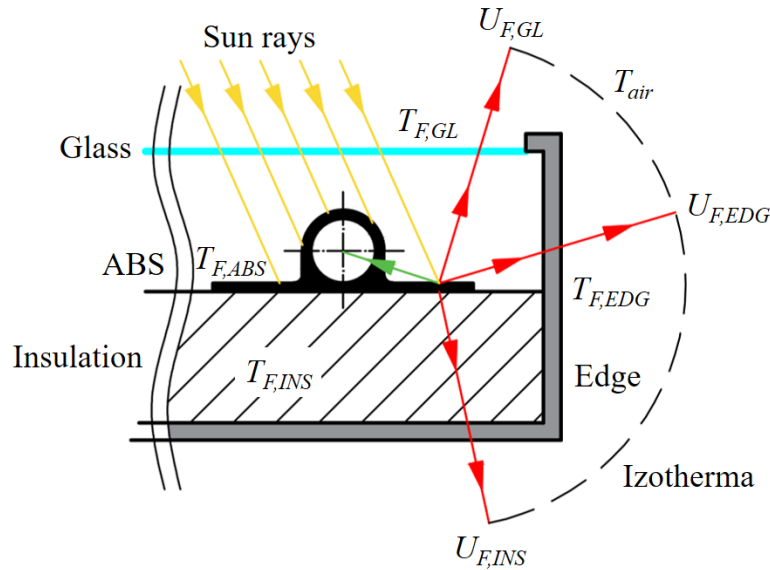
Fig. 3. Heat losses in the *fFPSC*.

Expressions for the $h_{F,ABS-GL(rad)}$ Eq. (15), and $h_{F,ABS-GL(con)}$ Eq. (16) transfer coefficients are taken from [37-39]:

$$h_{F,ABS-GL(rad)} = \cfrac{\sigma\left(T_{F,ABS}^2 + T_{F,GL}^2\right)\left(T_{F,ABS} + T_{F,GL}\right)}{\cfrac{1}{e_{F,ABS}} + \cfrac{1}{e_{F,GL}} - 1} \quad (15)$$

$$h_{F,ABS-GL(con)} = \frac{Nu_{F,AIR}k_{F,AIR}}{d_{F,AIR}} \tag{16}$$

where: σ [Wm^{-2}K^{-4}] is *Stefan-Boltzmann* constant, $T_{F,GL}$ [K] is the average temperature of the glass cover, $e_{F,ABS}$ [-] is the emission coefficient of the absorber, $e_{F,GL}$ [-] is the emission coefficient of the glass cover, $Nu_{F,AIR}$ [-] is the *Nusselt* number of the air layer, $k_{F,AIR}$ [Wm^{-1}K^{-1}] is the thermal conductivity of the air layer, and $d_{F,AIR}$ [m] is the thickness of the air layer.

To calculate the $h_{F,GL-air}$, it is necessary to first determine the $h_{F,GL-air(rad)}$ Eq. (17) [38], and second the $h_{F,GL-air(con)}$ Eq. (18) [41]:

$$h_{F,GL-air(rad)} = \sigma e_{F,GL}\left(T_{F,GL}^2 + T_{air}^2\right)\left(T_{F,GL} + T_{air}\right) \tag{17}$$

$$h_{F,GL-air(con)} = 2{,}8 + 3W \tag{18}$$

where W [ms^{-1}] is the wind speed.

The mentioned *fFPSC* characteristic surfaces (Fig. 4) $A_{F,ABS}$ Eq. (11), $A_{F,EDG}$ Eq. (14), and $A_{F,TOT}$ Eq. (14), are determined in the following ways Eqs. (19)-(21):

$$A_{F,ABS} = n_{F,ABS}L_{F,ABS(1)}u_{F,ABS} \tag{19}$$

$$A_{F,EDG} = 2\left(l_F L_F + l_F u_F\right) \tag{20}$$

$$A_{F,TOT} = 2\left(l_F L_F + l_F u_F + L_F u_F\right) \tag{21}$$

where: $n_{F,ABS}$ [-] is the number of absorber plates, $L_{F,ABS(1)}$ [m] is the width of one absorber plate, $u_{F,ABS}$ [m] is the length of one absorber plate, l_F [m] is the height of the *fFPSC*, L_F [m] is the width of the *fFPSC*, and u_F [m] is the length of the *fFPSC*.
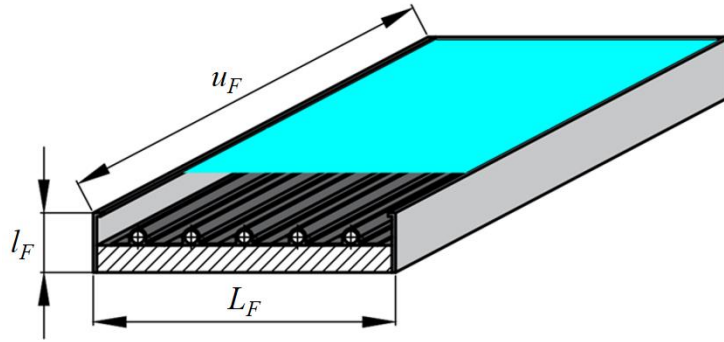
Fig. 4. Exterior dimensions of the *fFPSC*.

3.5. Heat power

The *fFPSC* heat power $Q_{F,HEAT}$ [W] Eq. (22) [39] is:

$$Q_{F,HEAT} = f_{F,HEAT}\left(A_{F,ABS(up)}I_{F,TOT} - \frac{T_{F,w(in)} - T_{air}}{\sum R_{F,LOSS}}\right) \tag{22}$$

where: $f_{F,HEAT}$ [-] is the heat energy transfer factor of the *fFPSC*, and $T_{F,w(in)}$ [K] is the average temperature of the water inlet.

3.6. Thermal efficiency

One of the most important indicators of the thermal performance of the *fFPSC* is its thermal efficiency η_F [-]. According to [37-39], the η_F can be theoretically determined using Eq. (23):

$$\eta_F = \frac{Q_{F,HEAT}}{Q_{F,SUN}} = \frac{f_{F,HEAT}\left(A_{F,ABS(up)}I_{F,TOT} - \dfrac{T_{F,w(in)} - T_{air}}{\sum R_{F,LOSS}}\right)}{A_{F,ABS(up)}I_{F,TOT}} \tag{23}$$

where $Q_{F,SUN}$ [W] is the incoming solar heat flux.

4. Materials and methods

4.1. Iterative procedure

The Fig. 5 shows a calculation algorithm based on a triple iterative procedure used in the phase of theoretical research of the *fFPSC* construction.
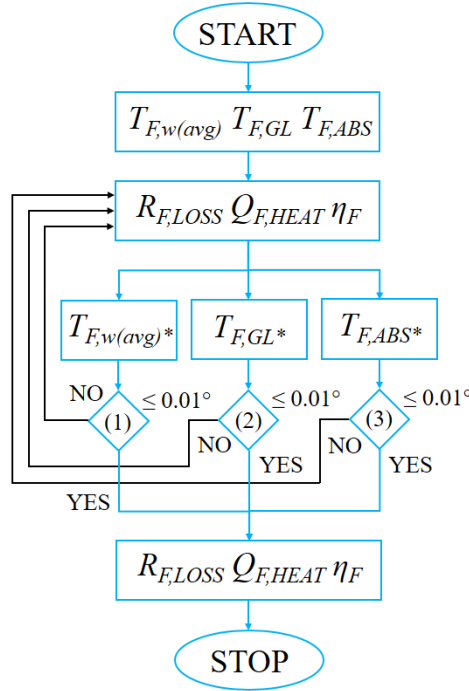
Fig. 5. Calculation algorithm for the *fFPSC*.

The theoretical research is based on the following imputations: [34] Q_z, $t_{F,w(in)}$, t_{air}, and W. These values were measured experimentally thanks to the meteorological station that the Faculty owns.

The calculation of the main thermal performances ($\Sigma R_{F,LOSS}$, $Q_{F,HEAT}$, and η_F) was based on the application of Eqs. (1)-(23), Chapter 3, with the initial assumption of characteristic temperatures ($t_{F,w(avg)}$, $t_{F,GL}$, and $t_{F,ABS}$), which, due to inaccessibility, are often not measured in practice.

After completing this calculation, all three assumed values were subjected to checks, ie. triple filtration (Fig. 5):

$$T_{F,w(avg)} = T_{F,w(in)} + \frac{Q_{F,HEAT}\sum R_{F,LOSS}}{A_{F,ABS(up)}f_{F,HEAT}}\left(1 - \frac{f_{F,HEAT}}{G_{F,HEAT}}\right) \tag{24}$$

$$T_{F,GL} = T_{F,ABS} - \frac{U_{F,GL}\left(T_{F,ABS} - T_{air}\right)}{h_{F,ABS-GL(rad)} + h_{F,ABS-GL(con)}} \qquad (25)$$

$$T_{F,ABS} = T_{F,w(in)} + \frac{Q_{F,HEAT}\left(1 - f_{F,HEAT}\right)\sum R_{F,LOSS}}{f_{F,HEAT}} \qquad (26)$$

where: $T_{F,w(avg)}$ [K] is the average temperature of the water of the *fFPSC*, and $G_{F,HEAT}$ [-] is the efficiency factor.

In the first iteration, Eq. (24) was used to determine the new value of $t_{F,w(avg)*}$. The new value of the mean water temperature would be compared with its previously calculated value. This (first) stage of the calculation would be completed when the following condition is fulfilled: $|t_{F,w(avg)*} - t_{F,w(avg)}| \leq 0.01$.

The second phase, applying Eq. (25), used the same method (procedure), which would last until $|t_{F,GL*} - t_{F,GL}| \leq 0.01$. The last iteration involved applying Eq. (26) until the absolute measurement error reached $|t_{F,ABS*} - t_{F,ABS}| \leq 0.01$.

By fulfilling all three conditions, the final output of $\Sigma R_{F,LOSS*}$, $Q_{F,HEAT*}$, η_{F*}, and $t_{F,w(out)*}$ was performed. This would complete the iterative procedure, and therefore the theoretical calculation of the thermal performance of the *fFPSC*.

4.2. SLR model

Based on the experimentally measured values [34], it is possible to make a relation between them and thus to make a prediction, in this case of the thermal behavior of the *fFPSC*. For this purpose, a large number of different numerical tools are available, among which is Simple Linear Regression (*SLR*).

SLR is a statistical method that is based on the mutual relationship between two quantitative variables, whereby the value of the dependent variable can be predicted on the basis of one independent variable. *SLR* is the simplest form of Linear Regression [42], which can be represented by the following general formula Eq. (27):

$$q_{F,HEAT} = x_1\, q_z + x_2 \qquad (27)$$

5. Results and discussion

5.1. Theoretical results

The results of the theoretical part of the research represent the validation of the heat power of the *fFPSC*, the parameter that was measured in the experimental part of the work [34].

Comparison between theoretical and experimental, i.e. measured values of heat power for the *fFPSC* are shown in the following order: for June 29 (Fig. 6), for June 30 (Fig. 7), and for July 15 (Fig. 8).

The average daily values of the *fFPSC* experimental specific heat powers for the analyzed days are [34] (Figs. 6-8): 381.78 Wm^{-2} (June 29), 364.33 Wm^{-2} (June 30), and 373.06 Wm^{-2} (July 15). The following average daily specific theoretical heat powers correspond to these values: 391.86 Wm^{-2} (June 29), 380.64 Wm^{-2} (June 30), and 387.46 Wm^{-2} (July 15).

During all three days (Figs. 6-8), moments were recorded when the theoretical heat power was greater than the experimental heat power, i.e. those were positive deviations, but also, there were moments when the experimental heat power was greater than the theoretical, which constitutes negative deviations. Positive deviations ranged in the following limits: June 29 (from 0.54% to 19.32%), June 30 (from 0.05% to 21.4%), and July 15 (from 0.26% to 30.11%). On the other hand, negative deviations were in the following range: June 29 (from -7.33% to -0.09%), June 30 (from -7.26% to -0.21%), and July 15 (from -7.41% to -0.1%).
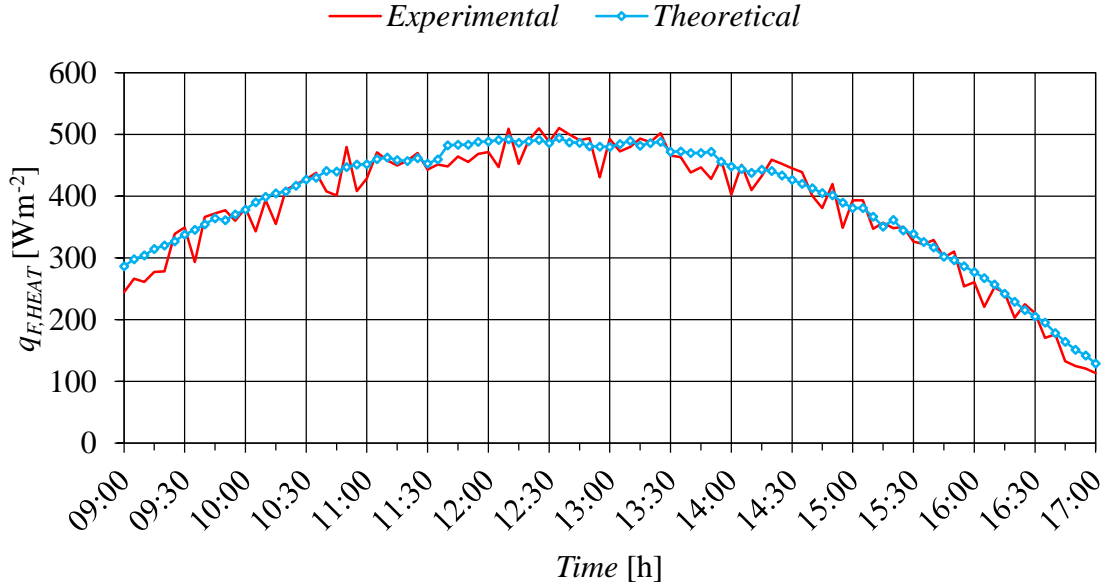
Fig. 6. Cpecific heat power validation results for the *fFPSC* (June 29).
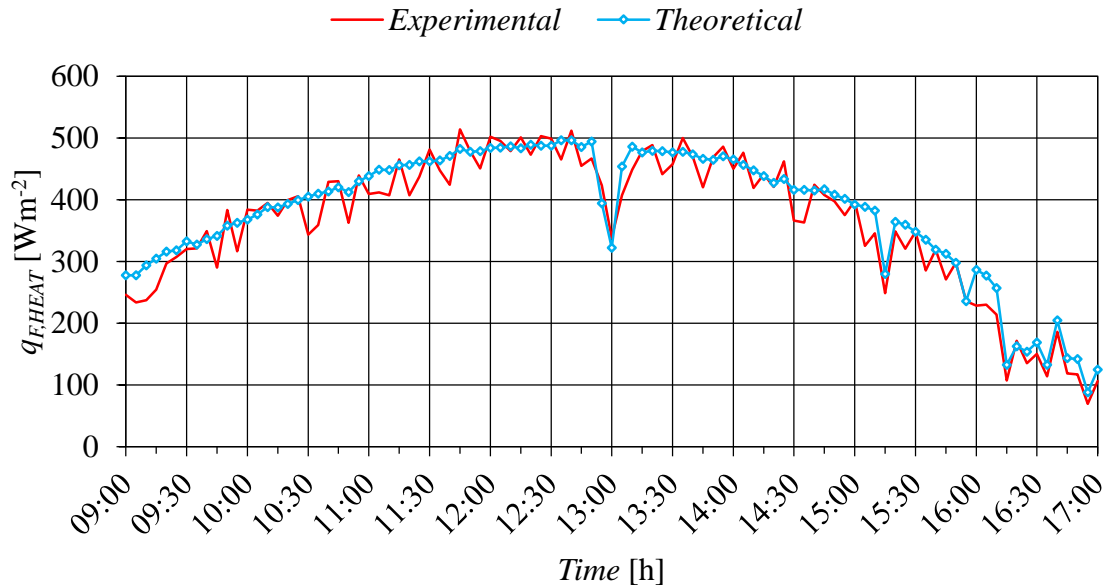
Fig. 7. Specific heat power validation results for the *fFPSC* (June 30).

One of the reasons for the deviation of the theoretical from the experimental model is the value of the mass flow rate. Namely, in the theoretical calculations, a constant, i.e. average value of mass flow was used, although the buoy in the upper water tank [34] could not ensure the constancy of the hydrostatic pressure throughout the day. In other words, there were also small variations in mass flow. The complexity of the mechanisms of heat propagation between the *SC* frame sides and the

surroundings must not be neglected either. The presence of dust on the glass cover surface, as a result of the influence of the wind, the turbidity of the atmosphere, and the accuracy of the measuring equipment also affected the theoretical model.
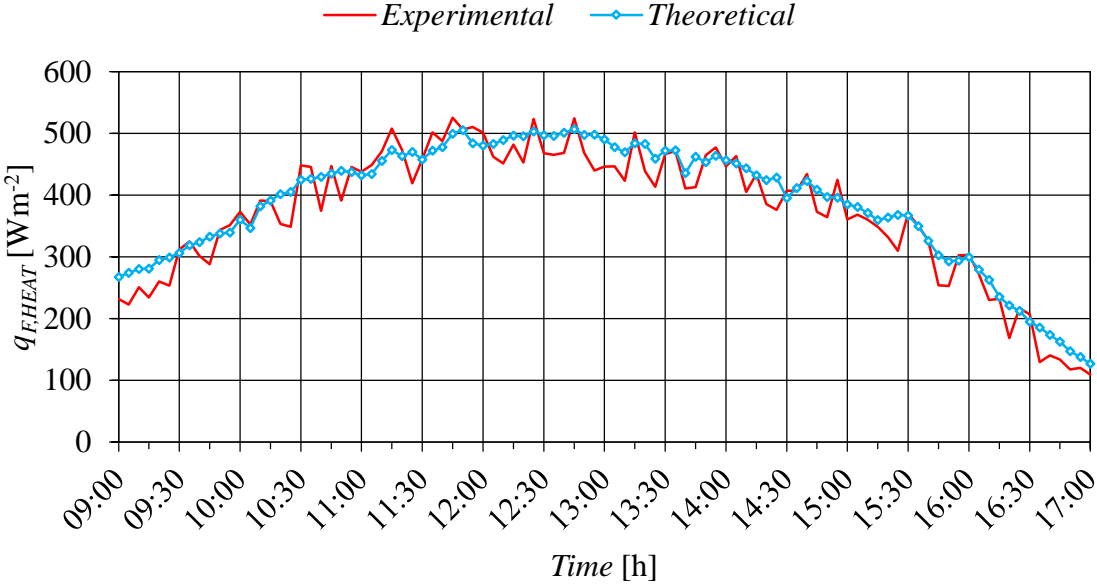
Fig. 8. Specific heat power validation results for the *fFPSC* (July 15).

It should also be noted, as can be seen from Figs. 6-8, that the biggest deviations were in the morning and evening hours, greater than 15% in favor of a theoretical model, when the surrounding shadows, still cold water at the *SC* inlet, and lower intensity of solar radiation had a greater impact on the performance of the *fFPSC*. The validation of the theoretical models has been confirmed thanks to the average daily deviations, in relation to the experimental measurements, which ranged within the following limits: June 29 (2.54%), June 30 (4.1%), and July 15 (3.84%).

Next figures (Figs. 9-11) show the water characteristic temperatures ($t_{F,w(in)}$, $t_{F,w(out)}$, and $\Delta t_{F,w}$), which are in accordance with the respective heat powers (Figs. 6-8).
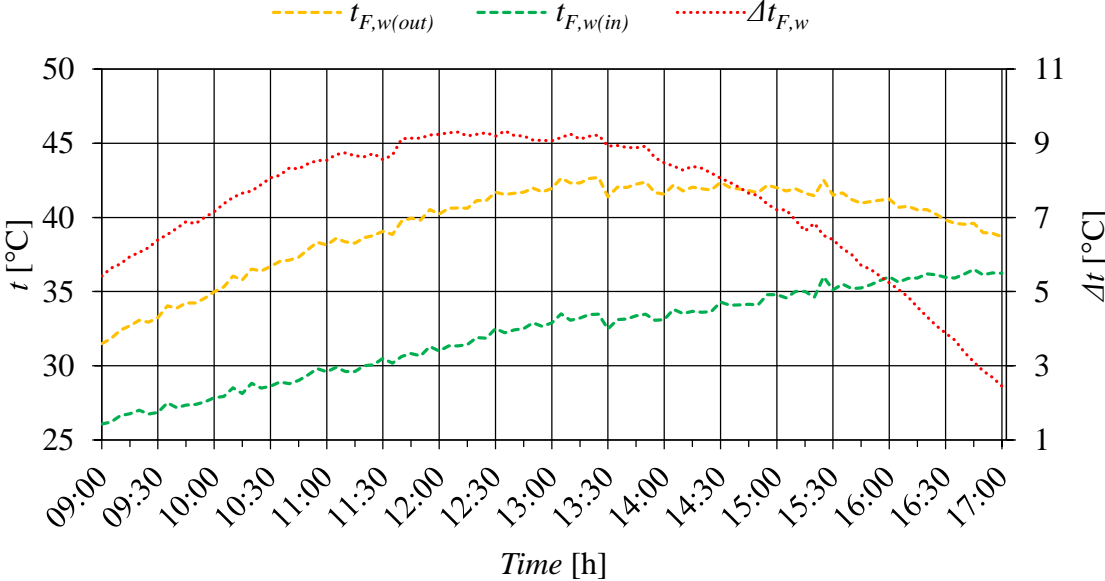
Fig. 9. Water characteristic temperatures for the *fFPSC* (June 29).
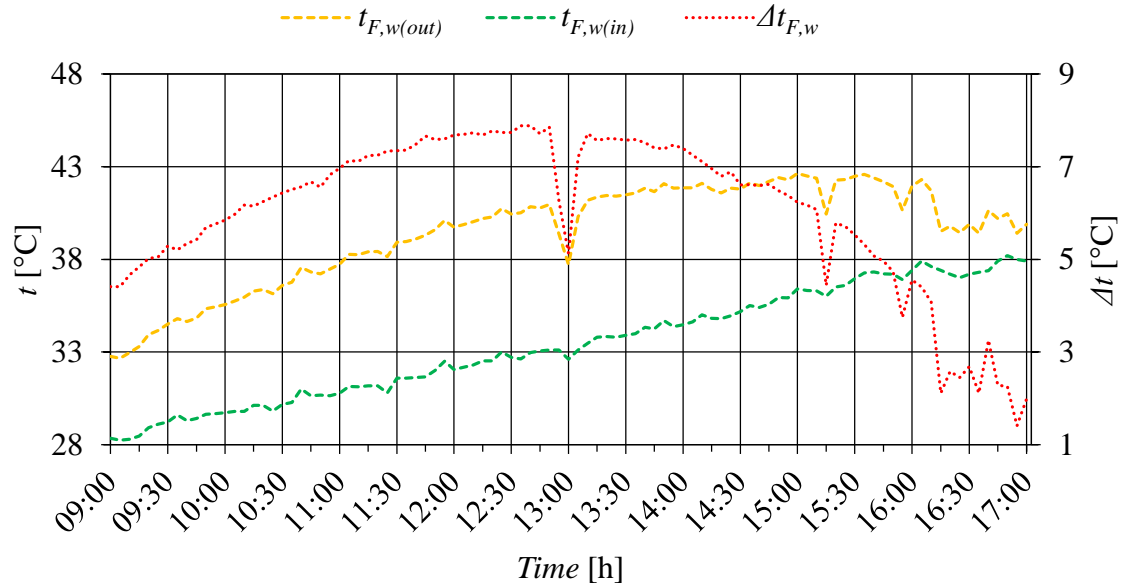
Fig. 10. Water characteristic temperatures for the *fFPSC* (June 30).
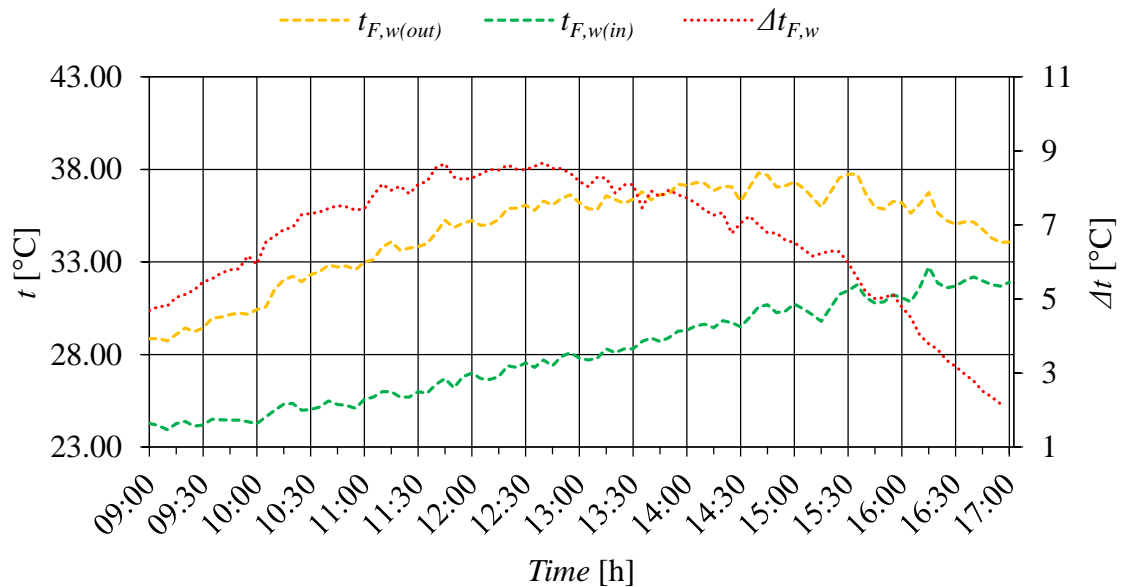
Fig. 11. Water characteristic temperatures for the *fFPSC* (July 15).

The first thing that can be observed from Figs. 9-11 is the daily change of the $t_{F,w(in)}$ (from 09:00 h to 17:00 h): June 29 (from 26.07 °C to 36.24 °C), June 30 (from 28.34 °C to 37.9 °C), and July 15 (from 24.29 °C to 32.73 °C). The following values $t_{F,w(out)}$ were recorded in the same moments of time in Figs. 9-11: June 29 (from 31.49 °C to 38.69 °C), June 30 (from 32.76 °C to 39.88 °C), and July 15 (from 28.87 °C to 34.08 °C). In the end, it can be concluded that the value $\Delta t_{F,w}$ moved (from 09:00 h to 17:00 h) in the following way (Figs. 9-11): June 29 (from 5.42 °C to 2.44 °C), June 30 (from 4.41 °C to 1.98 °C), and July 15 (from 4.58 °C to 2.17 °C).

5.2. Numerical results

Thermal analysis of the *fFPSC* can also be done using an *SLR*. The functional dependence between the (experimentally measured) solar radiation recorded by the pyranometer and (experimentally determine) heat power is shown in Figs. 12-14.
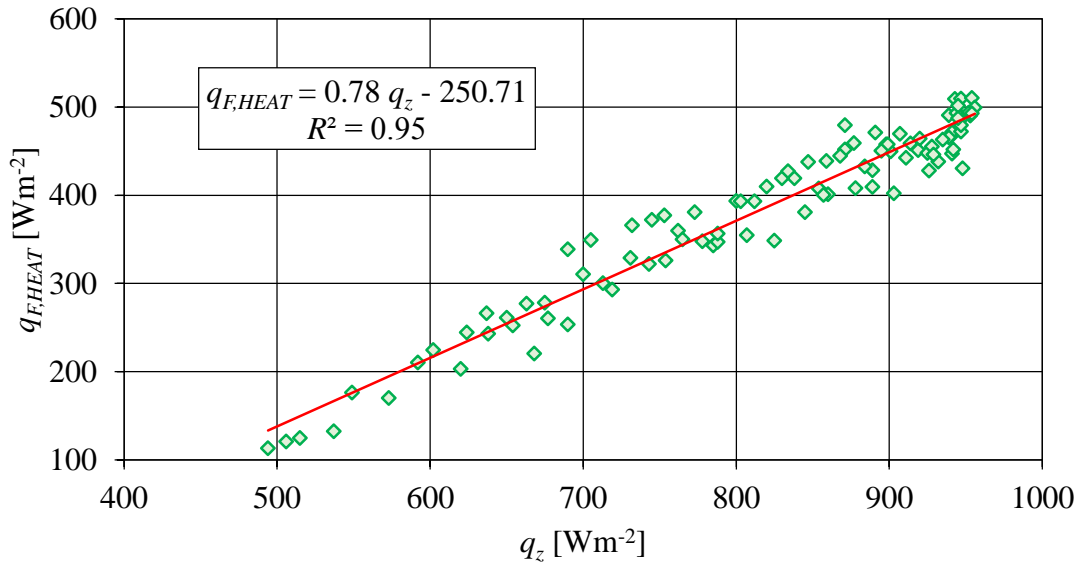
Fig. 12. Functional dependence between solar radiation and *fFPSC* heat power (June 29).

The coefficient of determination (R^2) of heat power, if only solar radiation is taken into account, shows satisfactory results ($R^2 > 0.9$ for all cases). The best (numerical) predictive results were achieved for June 29 ($R^2 = 0.95$). The second-best results were obtained on July 15 ($R^2 = 0.92$), while the worst results were achieved on June 30 ($R^2 = 0.91$).
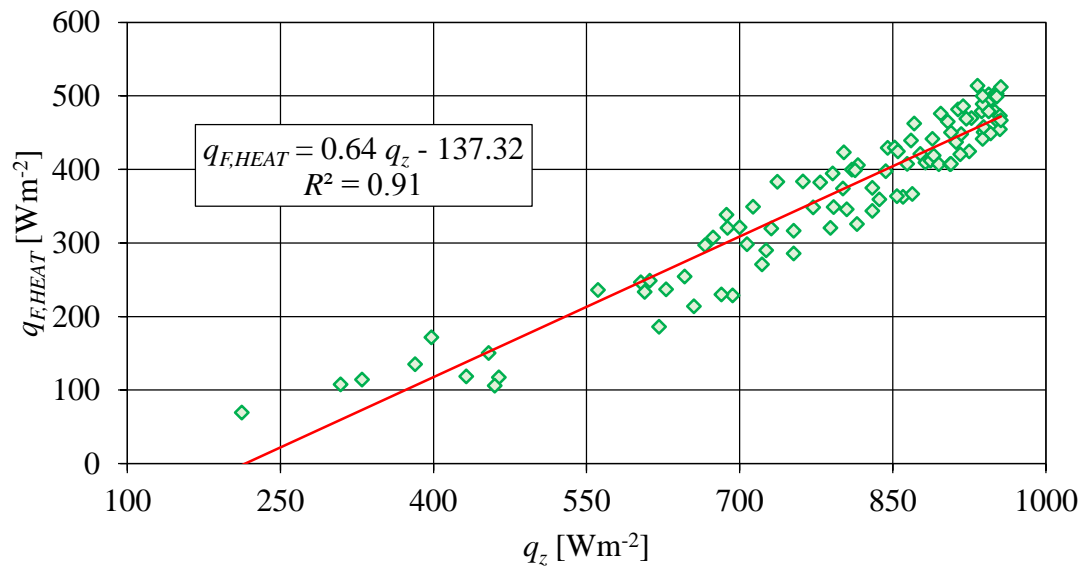
Fig. 13. Functional dependence between solar radiation and *fFPSC* heat power (June 30).

The biggest deviations of the numerical model can be observed at lower values of q_z, i.e. in the morning and evening hours. As already said, the conditions for conducting the experimental investigation on the roof of the Faculty [34] were specific, because behind the *fFPSC* there was a room that affected the operation of the solar installation in this period.

Based on the numerical results, one more interesting conclusion can be drawn. At lower values of solar radiation intensity ($q_z < 770$ Wm^{-2}), heat power in *fFPSC* decreases along with the q_z. On the other side, when is $q_z > 770$ Wm^{-2}, then the heat power in *fFPSC* increases along with the q_z. Up to this critical value of solar radiation intensity, $q_{F,HEAT} < 350$ Wm^{-2}. On the other hand, for values $770 < q_z < 950$ Wm^{-2}, the heat power is $350 < q_{F,HEAT} < 550$ Wm^{-2}. These effects are partly due to $t_{F,w(in)}$. Based on

Eq. (22) and Eq. (23) it can be concluded that the heat power of the *fFPSC* decreases (its heat losses increase) with the increase of the water inlet temperature.
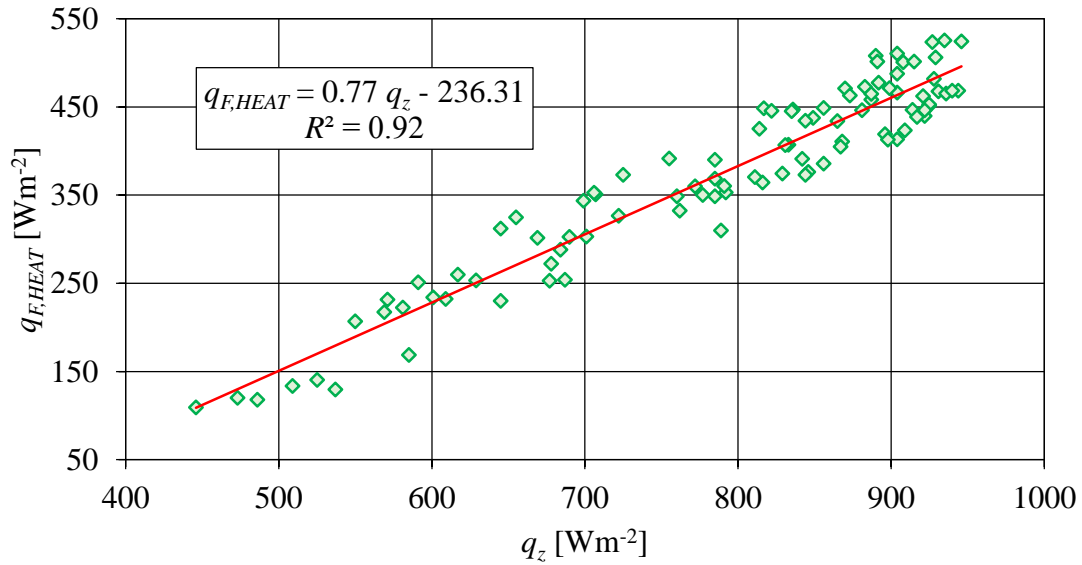
Fig. 14. Functional dependence between solar radiation and *fFPSC* heat power (July 15).

A comprehensive (theoretical and numerical, with previous experimental [34]) analysis of the *fFPSC* with *Sn-Al$_2$O$_3$* selective absorber and gravity water flow showed the justification of the application of this (and similar) *SCs* constructions, even in moments when the global energy-economic conditions are uncertain. In the constant search for new ways to provide sufficient amounts of energy, this is just one way it can be done.

6. Conclusion

After the initial (two-month) experimental investigations of the thermal performance of the *fFPSC* with a selective *Sn-Al$_2$O$_3$* absorber and gravity water flow, in this work, the investigation of the mentioned solar construction is completed, by applying additional methods: theoretical and numerical. In the theoretical part, the equations for the mathematical determination of the *fFPSC* thermal characteristics are presented in detail. In this phase, an algorithm with a threefold iterative procedure was elaborated and presented. Numerical research was based on the application of the well-known *SLR* method. The role of the independent variable was the solar radiation intensity on the horizontal surface, while the calculation of the heat power represented the objective function.

The theoretical research resulted in the following values of average daily specific heat powers: 391.86 Wm^{-2} (June 29), 380.64 Wm^{-2} (June 30), and 387.46 Wm^{-2} (July 15). The theoretical model was verified because the absolute measurement error for all analyzed days was less than 10%. Numerical results also showed agreement between (experimentally determine) heat power and solar radiation (experimentally measured), because the coefficient of determination during all test days was greater than 90%.

This study proved that the practical use of the *fFPSCs* without circulation pumps (additional energy investment) could be relatively useful in temperate continental climate conditions. The goal of the paper is to show that more attention should be paid to the development of solar devices that do not require electricity. In this way, their application in the industrial, residential, and agricultural sectors would increase even more, which would ultimately have positive effects on the environment.

Acknowledgment

Nomenclature:

A – Area, [m^2]

a – Absorption coefficient, [-]

alb – Ground albedo, [-]

d – Thickness, [m]

e – Emission coefficient, [-]

f – Heat energy transfer factor, [-]

G – Efficiency factor, [-]

h – Convective (and radiation) transfer coefficient, [Wm^{-2}K^{-1}]

I – Solar radiation, [Wm^{-2}]

k – Thermal conductivity, [Wm^{-1}K^{-1}]

L – Width, [m]

l – Height, [m]

n – Number, [-]

Nu – *Nusselt* number, [-]

Q – Heat flux, [W]

q – Specific heat flux, [Wm^{-2}]

R – Resistance to heat transfer, [KW^{-1}]

T – Absolute temperature, [K]

t – Temperature, [°C]

U – Heat transfer coefficient, [Wm^{-2}K^{-1}]

u – Lenght, [m]

W – Wind speed, [ms^{-1}]

Greek letters:

β – Inclination angle, [°]

δ – Declination, [°]

η – Efficiency, [-]

θ – Solar incident angle, [°]

σ – *Stefan-Boltzmann* constant, [Wm^{-2}K^{-4}]

τ – Transparency coefficient, [-]

φ – Latitude, [°]

ω – Hour angle, [°]

Subscripts:

ABS – Absorber

AIR – Air layer (Interior air)
air – Ambient (exterior) air
avg – Average
B – Beam modifier
BEAM – Beam
con – Convection
D – Diffuse modifier
DIFF – Diffuse
EDG – Side edges
F – FPSC
GL – Glass cover
HEAT – Useful heat
in – Inlet
INS – Insulation
LOSS – Heat losses
rad – Radiation
R – Reflection modifier
REFL – Reflected
SUN – Solar
TOT – Total
up – Upside
w – Water
z – Horizontal
$\perp$ – Normal
* – Corection

Abbreviations:

DAT – Double-axis tracking
FPSC – Flat-plate *SC*
fFPSC – Fixed *FPSC*
SAT – Single-axis tracking
SC – Solar collector

References:

[1] Ibrahim, A., Kocak, S., Theoretical energy and exergy analyses of solar assisted heat pump space heating system, *Thermal Science*, 18 (2014), 2, pp. S417-S427, Doi: 10.2298/TSCI120813024A.

[2] Solanki, A., Yash, P., Applications of a flat plate collector in dairy industries: A review, *International Journal of Ambient Energy*, 43 (2022), 1, pp. 1915-1923, Doi: 10.1080/01430750.2020.1721326.

[3] Nešović, A., Theoretical model of solar incident angle for an optionally oriented fixed flat surface, *Technique*, 77 (2022), 3, pp. 328-333, Doi: 10.5937/tehnika2203328N.

[4] Wazwaz, A., *et. al.*, Solar thermal performance of a nickel-pigmented aluminium oxide selective absorber, *Renewable Energy*, 27 (2002), 2, pp. 277-292, Doi: 10.1016/S0960-1481(01)00192-6.

[5] Wazwaz, A., *et. al.*, The effects of nickel-pigmented aluminium oxide selective coating over aluminium alloy on the optical properties and thermal efficiency of the selective absorber prepared by alternate and reverse periodic plating technique, *Energy Conversion and Management*, 51 (2010), 8, pp. 1679-1683, Doi: 10.1016/j.enconman.2009.11.047.

[6] Li, Z., *et. al.*, Aqueous solution-chemical derived Ni-Al2O3 solar selective absorbing coatings, *Solar Energy Materials and Solar Cells*, 105 (2012), No, pp. 90-95, Doi: 10.1016/j.solmat.2012.05.030.

[7] Xue, Y., *et. al.*, Spectral properties and thermal stability of solar selective absorbing AlNi-Al2O3 cermet coating, *Solar Energy*, 96 (2013), No, pp. 113-118, Doi: 10.1016/j.solener.2013.07.012.

[8] Teixeira V., *et. al.*, Spectrally selective composite coatings of Cr-Cr2O3 and Mo-Al2O3 for solar energy applications, *Thin Solid Films*, 392 (2001), 2, pp. 320-326, Doi: 10.1016/S0040-6090(01)01051-3.

[9] Xinkang, D., *et. al.*, Microstructure and spectral selectivity of Mo-Al2O3 solar selective absorbing coatings after annealing, *Thin Solid Films*, 516 (2008), 12, pp. 3971-3977, Doi: 10.1016/j.tsf.2007.07.193.

[10] Antonaia, A., *et. al.*, Stability of W-Al2O3 cermet based solar coating for receiver tube operating at high temperature, *Solar Energy Materials and Solar Cells*, 94 (2010), 10, pp. 1604-1611, Doi: 10.1016/j.solmat.2010.04.080.

[11] Ding, D., *et. al.*, Optical, structural and thermal characteristics of Cu-CuAl2O4 hybrids deposited in anodic aluminum oxide as selective solar absorber, *Solar Energy Materials and Solar Cells*, 94 (2010), 10, pp. 1578-1581, Doi: 10.1016/j.solmat.2010.04.075.

[12] Nuru, Z. Y., *et. al.*, Pt-Al2O3 nanocoatings for high temperature concentrated solar thermal power applications, *Physica B: Condensed Matter*, 407 (2012), 10, pp. 1634-1637, Doi: 10.1016/j.physb.2011.09.104.

[13] Barshilia, H. C., *et. al.*, Structure and optical properties of Ag-Al2O3 nanocermet solar selective coatings prepared using unbalanced magnetron sputtering, *Solar Energy Materials and Solar Cells*, 95 (2011), 7, pp. 1707-1715, Doi: 10.1016/j.solmat.2011.01.034.

[14] Chorchong, T., *et. al.*, Characterization and spectral selectivity of Sn-Al2O3 solar absorber, *Key Engineering Materials*, 675 (2016), No, pp. 467-472, Doi: 10.4028/www.scientific.net/KEM.675-676.467.

[15] Wamae, W., *et. al.*, Influence of tin content on spectral selectivity and thermal conductivity of Sn-Al2O3 solar selective absorber, *Materials for Renewable and Sustainable Energy*, 7 (2018), No, pp. 1-8, Doi: 10.1007/s40243-017-0109-1.

[16] Wamae, W., *et. al.*, Thermal efficiency of a new prototype of evacuated tube collector using Sn-Al2O3 as a selective solar absorber, *Walailak Journal of Science and Technology*, 15 (2018), 11, pp. 793-802, Doi: 10.48048/wjst.2018.5965.

[17]   Alvarez, A., *et. al.*, Experimental and numerical investigation of a flat-plate solar collector, *Energy*, 35 (2010), 9, pp. 3707-3716, Doi: 10.1016/j.energy.2010.05.016

[18]   Hellstrom, B., *et. al.*, The impact of optical and thermal properties on the performance of flat plate solar collectors, *Renewable Energy*, 28 (2003), 3, pp. 331-344, Doi: 10.1016/S0960-1481(02)00040-X.

[19]   Shemelin, V., Matuska, T., Detailed modeling of flat plate solar collector with vacuum glazing, *International Journal of Photoenergy*, No (2017), No, pp. 1-9, Doi: 10.1155/2017/1587592.

[20]   Khoukhi, M., *et. al.*, Flat-plate solar collector performance with coated and uncoated glass cover, *Heat Transfer Engineering*, 27 (2006), 1, pp. 46-53, Doi: 10.1080/01457630500343009.

[21]   Akhtar, N., Mullick, S. C., Computation of glass-cover temperatures and top heat loss coefficient of flat-plate solar collectors with double glazing, *Energy*, 32 (2007), 7, pp. 1067-1074, Doi: 10.1016/j.energy.2006.07.007.

[22]   Subiantoro, A., Ooi, K. T., Analytical models for the computation and optimization of single and double glazing flat plate solar collectors with normal and small air gap spacing, *Applied Energy*, 104 (2013), No, pp. 392-399, Doi: 10.1016/j.apenergy.2012.11.009.

[23]   Chen, C. Q., *et. al.*, Numerical evaluation of the thermal performance of different types of double glazing flat-plate solar air collectors, *Energy*, 233 (2021), No, pp. 121087, Doi: 10.1016/j.energy.2021.121087.

[24]   Vettrivel, H., Mathiazhagan, P., Comparison study of solar flat plate collector with single and double glazing systems, *International Journal of Renewable Energy Research*, 7 (2017), 1, pp. 266-274, Doi: 10.20508/ijrer.v7i1.5397.g6985.

[25]   Baccoli, R., *et. al.*, A mathematical model of a solar collector augmented by a flat plate above reflector: Optimum inclination of collector and reflector, *Energy Procedia*, 81 (2015), No, pp. 205-214, Doi: 10.1016/j.egypro.2015.12.085.

[26]   Baccoli, R., *et. al.*, A comprehensive optimization model for flat solar collector coupled with a flat booster bottom reflector based on an exact finite length simulation model, *Energy Conversion and Management*, 164 (2018), No, pp. 482-507, Doi: 10.1016/j.enconman.2018.02.091.

[27]   Chiam, H. F., Planar concentrators for flat-plate solar collectors, *Solar Energy*, 26 (1981), 6, pp. 503-509, Doi: 10.1016/0038-092X(81)90161-4.

[28]   Larson, D. C., Mirror enclosures for double-exposure solar collectors, *Solar Energy*, 23 (1979), 6, pp. 517-524, Doi: 10.1016/0038-092X(79)90076-8.

[29]   Nikolić, N., Lukić, N., A mathematical model for determining the optimal reflector position of a double exposure flat-plate solar collector, *Renewable Energy*, 51 (2013), No, pp. 292-301, Doi: 10.1016/j.renene.2012.09.034.

[30]   Maia, C. B., *et. al.*, Evaluation of a tracking flat-plate solar collector in Brazil, *Applied Thermal Engineering*, 73 (2014), 1, pp. 953-962, Doi: 10.1016/j.applthermaleng.2014.08.052.

[31]   Neville, R. C., Solar energy collector orientation and tracking mode, *Solar Energy*, 20 (1978), 1, pp. 7-11, Doi: 10.1016/0038-092X(78)90134-2.

[32]   Drago, P., A simulated comparison of the useful energy gain in a fixed and a fully tracking flat plate collector, *Proceedings of the International Symposium – Workshop on Solar Energy*, Cairo, Egypt, 1980, Vol. No, pp. 258-273.

[33]   Attalage, R. A., Agami, R. T., Annual collectible energy of a two-axis tracking flat-plate solar collector, *Solar Energy*, 48 (1992), 3, pp. 151-155, Doi: 10.1016/0038-092X(92)90133-U.

[34]   Nešović, A., *et. al.*, Experimental analysis of the fixed flat-plate solar collector with Sn-Al2O3 selective absorber and gravity water flow, *Thermal Science*, 27 (2023), 1A, pp. 349-358, Doi: 10.2298/TSCI220904171N.

[35]   Beckman, W. A., *et. al.*, Solar heating design, by the f-chart method, *NASA STI/Recon Technical Report A*, 78 (1977), No, pp. 31071, Doi: No.

[36]   Mehregan, M., *et. al.*, Energy, economic, environmental investigations and optimization of a combined cooling, heating and power system with hybrid prime mover of gas engine and flat plate solar collector, *Energy Conversion and Management*, 251 (2022), No, pp. 115018, Doi: 10.1016/j.enconman.2021.115018.

[37]   Rabl, A., *Active solar collectors and their applications*, Oxford University Press on Demand, Oxford, UK, 1985.

[38]   Kalogirou, S. A., Solar thermal collectors and applications, *Progress in Energy and Combustion Science*, 30 (2004), 3, pp. 231-295, Doi: 10.1016/j.pecs.2004.02.001.

[39]   Stine, W. B., Harrigan, R. W., *Solar energy fundamentals and design*, Wiley-Interscience, New York, USA, 1985.

[40]   Wang, D., *et. al.*, Thermal performance analysis of large-scale flat plate solar collectors and regional applicability in China, *Energy*, 238 (2022), No, pp. 121931, Doi: 10.1016/j.energy.2021.121931.

[41]   Ali, S. H., *et. al.*, Energetic and exegetic performance analysis of flat plate solar collector under variables heat transfer coefficient and inlet water temperature, *Case Studies in Thermal Engineering*, 28 (2021), No, pp. 101700, Doi: 10.1016/j.csite.2021.101700.

[42]   Jurišević, N., System for monitoring and targeting of energy and water consumption in pubic buildings, Ph. D. thesis, University of Kragujevac, Kragujevac, SRB, 2021.